



# Controllable location of Au nanoparticles as cocatalyst onto $\text{TiO}_2/\text{CeO}_2$ nanocomposite hollow spheres for enhancing photocatalytic activity

Jiabai Cai<sup>a</sup>, Xueqing Wu<sup>a</sup>, Shunxing Li<sup>a,b,\*</sup>, Fengying Zheng<sup>a,b</sup>

<sup>a</sup> College of Chemistry and Environment, Minnan Normal University, Zhangzhou, 363000, PR China

<sup>b</sup> Fujian Province Key Laboratory of Modern Analytical Science and Separation Technology, Minnan Normal University, Zhangzhou, 363000, PR China

## ARTICLE INFO

### Article history:

Received 27 March 2016

Received in revised form 25 July 2016

Accepted 2 August 2016

Available online 2 August 2016

### Keywords:

Titania-based nanocomposite

Cocatalyst

Hollow structure

Sandwich

Photocatalysis

## ABSTRACT

Visible-light-driven photocatalysis as a green technology has attracted a lot of attention due to its potential applications in environmental remediation. Although  $\text{TiO}_2$  is the most popular photocatalyst, the lack of visible light utilization and a low efficiency of electron-hole separation should be overcome. Therefore, Au nanoparticles (NPs) as cocatalyst were controllably loaded between the double-shell or into  $\text{CeO}_2$  shell (as photocatalyst and oxygen buffer) and then a novel visible-light-driven  $\text{TiO}_2/\text{CeO}_2$  nanocomposite was prepared, using functionalized polystyrene spheres, sol-gel, hydrothermal reaction, and calcination. The presence of  $\text{TiO}_2$  shell, Au NPs and  $\text{CeO}_2$  shell were confirmed by EDX and electron energy loss mapping analysis. Under visible-light irradiation, the photo-degradation rate constant  $k$  ( $\text{min}^{-1}$ ) was in the order of  $\text{TiO}_2/\text{Au@CeO}_2$  (0.026) >  $\text{TiO}_2/\text{CeO}_2/\text{Au}$  (0.021) >  $\text{TiO}_2/\text{CeO}_2$  (0.014) >  $\text{CeO}_2$  (0.0091) >  $\text{TiO}_2$  (0.0046) > P25 (0.0034). Compared with P25,  $\text{TiO}_2/\text{CeO}_2$ , and  $\text{TiO}_2/\text{CeO}_2/\text{Au}$ , the visible-light photocatalytic activity of  $\text{TiO}_2/\text{Au@CeO}_2$  for the photo-degradation of organic pollutant and photo-reduction of  $\text{Cr(VI)}$  were the highest. This result was attributed to the combination of  $\text{TiO}_2$  and  $\text{CeO}_2$ , the double-shelled and sandwiched nanostructure and the addition of Au NPs as electron trap site and surface plasmon resonance-sensitizer, which could reduce the recombination of the electron-hole and induce the visible light absorption. The major obstacle of heterogeneous photocatalysis could be resolved. The photo-degradation rate of 95% was achieved by  $\text{TiO}_2/\text{Au@CeO}_2$ , which exhibited an increase of 63% compared to Degussa P25  $\text{TiO}_2$ . The photo-degradation activity of  $\text{TiO}_2/\text{CeO}_2/\text{Au}$  was improved by Au NPs loaded on outer shell of  $\text{TiO}_2/\text{CeO}_2/\text{Au}$  but limited by their stability. This work confirmed the importance of controllable location of the noble metals as cocatalysts.

© 2016 Elsevier B.V. All rights reserved.

## 1. Introduction

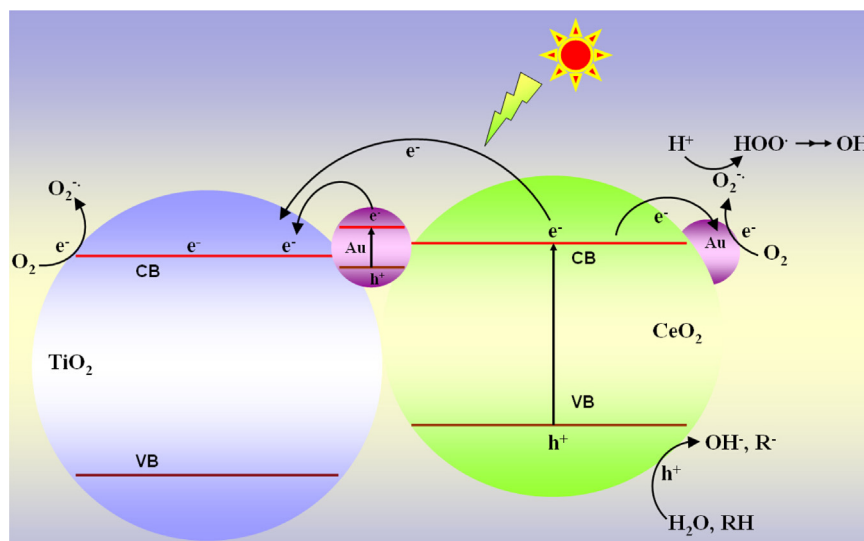
In recent years, photocatalytic degradation as an efficient and environment-friendly technology for organic pollutant removal has been attracted extensively attention [1–5]. Many metal-oxide photocatalysts have enabled great advances in the decomposition of pollutants under light irradiation [6–9]. Recently, it has been realized that the structure and morphology of the photocatalysts have significant effects on the photocatalytic activity [10–12]. As an efficient structure of metal oxide-based photocatalyst, hollow sphere has been used for its unique large surface area, low density, and efficient light-harvesting [13,14]. The surface plasmon resonance

(SPR) of Au nanoparticles (Au NPs) supported on semiconductors results in strong photo-absorption in the visible region which can be advantageous to improve photocatalytic activity [15]. Therefore, it is necessary to develop a new hollow sphere with supported Au NPs as a light-driven photocatalyst. However, the influence of Au NPs location site on the photocatalytic activity is unknown.

Among various inorganic oxide catalysts,  $\text{CeO}_2$  has attracted extensive interest due to its high thermal stability, oxygen storage capacities, and easy conversion between  $\text{Ce(III)}$  and  $\text{Ce(IV)}$  oxidation states. Specifically,  $\text{CeO}_2$  can act as an oxygen buffer by releasing/restoring oxygen, which plays an important role in many oxidation reactions [16–19]. As one of the most important metal oxides and semiconductors, titanium dioxide ( $\text{TiO}_2$ ), especially anatase  $\text{TiO}_2$ , has been used for photocatalysis, lithium-ion batteries, and solar cells. [20–22]. After  $\text{CeO}_2$ -doping, the light absorption property and photo-degradation performance of  $\text{TiO}_2$  are improved. Therefore,  $\text{TiO}_2\text{--CeO}_2$  nanocomposites with various

\* Corresponding author at: College of Chemistry and Environment, Minnan Normal University, Zhangzhou, 363000, PR China.

E-mail addresses: [shunxing.li@aliyun.com](mailto:shunxing.li@aliyun.com), [lshunxing@mnnu.edu.cn](mailto:lshunxing@mnnu.edu.cn) (S. Li).



**Scheme 1.** Charge transfers in  $\text{TiO}_2@\text{Au}@\text{CeO}_2$  composites.

morphologies have been used for photocatalysis, including core-shelled spheroids [23,24], nanosphere arrays [25,26], nanofibers [27], films [28,29], and nanoparticles [30–33]. Coupling of the band-gap excitation of  $\text{TiO}_2$  (or  $\text{CeO}_2$ ) and the SPR of Au NPs in  $\text{Au}/\text{TiO}_2$  (or  $\text{Au}/\text{CeO}_2$ ) sample, solar light can be effectively utilized [34,35]. Furthermore, the structure of double-shelled hollow spheres can accelerate efficiently the separation and transfer of photon-induced electrons and holes as well as increase the efficiency of the photocatalysis process [15,36–39]. Therefore, hollow sphere for  $\text{TiO}_2@\text{Au}@\text{CeO}_2$  and  $\text{TiO}_2@\text{CeO}_2/\text{Au}$  nanocomposite is proposed by the paper, furthermore to discover the important of controllable location of Au NPs.

Using polystyrene spheres (PS) as sacrificial templates, the nanoparticles of  $\text{TiO}_2$ , Au and  $\text{CeO}_2$  are coated successively onto PS. The resulted  $\text{PS}@\text{TiO}_2@\text{Au}@\text{CeO}_2$  and  $\text{PS}@\text{TiO}_2@\text{CeO}_2/\text{Au}$  nanocomposites are calcined at elevated temperature, and then double-shelled  $\text{TiO}_2@\text{Au}@\text{CeO}_2$  and  $\text{TiO}_2@\text{CeO}_2/\text{Au}$  hollow spheres are obtained. As electron trap site and SPR-sensitizer, Au NPs in the  $\text{TiO}_2@\text{Au}@\text{CeO}_2$  or  $\text{TiO}_2@\text{CeO}_2/\text{Au}$  can reduce the recombination of the electron-hole separation. Moreover, the visible light absorption of  $\text{TiO}_2@\text{Au}@\text{CeO}_2$  and  $\text{TiO}_2@\text{CeO}_2/\text{Au}$  hollow spheres can be increased by the coexistence of Au NPs, and then the major obstacle of heterogeneous photocatalysis can be resolved. The work intensifies the fundamental of understanding the controllable location of noble metals as cocatalysts for enhancing photocatalytic activity (Scheme 1).

## 2. Experimental section

### 2.1. Reagents and chemicals

Tetrabutyl titanate (TBOT, 99%) was purchased from J&K Chemistry Co. Ltd. ( $\text{CeN}_3\text{O}_9 \cdot 6\text{H}_2\text{O}$ , 99.8%) was purchased from Aladdin Chemistry Co. Ltd. G-glucose ( $\text{C}_6\text{H}_{12}\text{O}_6 \cdot \text{H}_2\text{O}$ , 99%), urea ( $\text{H}_2\text{NCONH}_2$ , 99%), sodium persulfate ( $\text{Na}_2\text{S}_2\text{O}_8$ , 98%), trisodium citrate dihydrate ( $\text{C}_6\text{H}_{12}\text{O}_7\text{Na}_3 \cdot 2\text{H}_2\text{O}$ , 99%), and ethanol ( $\text{C}_2\text{H}_6\text{O}$ , 99.7%) were purchased from Guangzhou Xilong Chemistry Technology Co. Ltd and used without additional purification. Tetrachloroauric (III) acid hydrate ( $\text{AuCl}_3 \cdot \text{HCl} \cdot 4\text{H}_2\text{O}$ , 99%), methyl acrylate ( $\text{C}_4\text{H}_6\text{O}_2$ , 98%) and styrene ( $\text{C}_8\text{H}_8$ , 99%) were purchased from Shanghai Sinopharm Chemistry Co. Ltd and used without additional purification. Distilled water was used in the catalyst preparation and subsequent catalytic tests.

### 2.2. Synthesis of $\text{CeO}_2$ nanoparticles

1 g of glucose and 0.22 g of urea were dissolved in 10 mL of deionized water to form a clear solution and 0.1 g of  $\text{CeN}_3\text{O}_9 \cdot 6\text{H}_2\text{O}$  was added to above solution. The mixture was transferred to Teflon-lined stainless steel autoclaves and heated to 160 °C for 20 h. The resulting nanoparticles were washed three times with ethanol and dried in vacuum at 60 °C for 6 h. Finally, heated with a rate of 5 °C/min and maintained at 600 °C (i.e., calcination temperature) for 6 h in static air. The  $\text{CeO}_2$  nanoparticles were finally obtained.

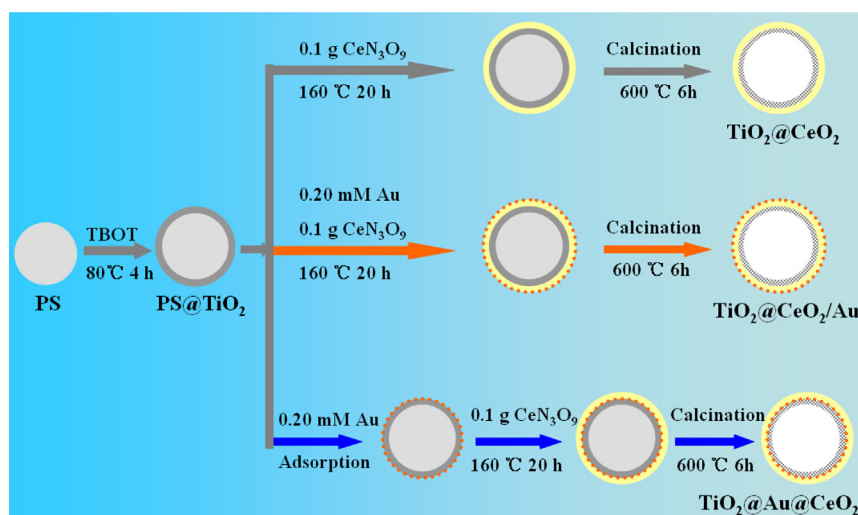
### 2.3. Synthesis of $\text{TiO}_2@\text{CeO}_2$ , $\text{TiO}_2@\text{CeO}_2/\text{Au}$ , and $\text{TiO}_2@\text{Au}@\text{CeO}_2$ hollow spheres

$\text{PS}@\text{TiO}_2$  nanocomposite (0.05 g) was added into the ethanol solution (50 mL) under vigorous stirring for 15 min, and the mixture was named as solution A. Glucose (1 g) and urea (0.22 g) were dissolved in deionized water (10 mL) and  $\text{CeN}_3\text{O}_9 \cdot 6\text{H}_2\text{O}$  (0.1 g) was added to above solution. The resulting mixture was kept for 15 min under stirring and the mixture was named as solution B. The solution B was added drop by drop into the solution A under vigorous stirring for 15 min. Then, the mixture was transferred to Teflon-lined stainless steel autoclaves and heated to 160 °C for 20 h. The resulting nanoparticles were washed three times with ethanol and dried in vacuum at 60 °C for 6 h. Finally, heated with a rate of 5 °C/min and maintained at 600 °C (i.e., calcination temperature) for 6 h in static air. The  $\text{TiO}_2@\text{CeO}_2$  hollow spheres were finally obtained.

For comparison, the  $\text{TiO}_2@\text{CeO}_2/\text{Au}$  and  $\text{TiO}_2@\text{Au}@\text{CeO}_2$  hollow spheres were also prepared by the similar experimental procedure. The difference was the addition of the prepared Au NPs (5 nm, 0.20 mM, 3 mL) under stirring for 2 h, but the adding sequences were different (see Scheme 2). Au NPs were added into solution B and mixed with  $\text{CeN}_3\text{O}_9$  for  $\text{TiO}_2@\text{CeO}_2/\text{Au}$ . After Au NPs were adsorbed onto  $\text{PS}@\text{TiO}_2$ ,  $\text{CeN}_3\text{O}_9$  in the solution B was added for  $\text{TiO}_2@\text{Au}@\text{CeO}_2$ .

### 2.4. Characterization

The morphology of nanocomposite samples was observed on S-4800 scanning electron microscopy (SEM) instrument (Hitachi, Japan). Transmission electron microscopy (TEM) images were recorded on JEM-2100 (HR) microscope (JEOL, Japan) operated at



**Scheme 2.** A general “template + sol-gel + calcination” method for preparing the double-shelled  $\text{TiO}_2@\text{CeO}_2$ ,  $\text{TiO}_2@\text{CeO}_2/\text{Au}$ ,  $\text{TiO}_2@\text{Au}@\text{CeO}_2$  nanocomposites.

200 kV. Elemental mapping image, the line scanning image, and EDX analysis, performed on a Tecnai G<sup>2</sup> F20 U-TWIN microscope (FEI, America), were used to prove the independent presence of  $\text{TiO}_2$  shell,  $\text{CeO}_2$  shell, and supported Au NPs. The distribution of elements in a specimen was clarified by selecting and imaging the electrons with a specific energy loss. Powder X-ray diffraction data (XRD) were recorded on a Rigaku D/MAX-TTRIII (CBO) X-ray diffractometer at 40 kV and 30 mA for monochromatic Cu K $\alpha$  radiation in the range of 20°–80°. Thermo-gravimetric analysis (TG) was performed on a TG 2009F1 analyzer (NETZSCH, Germany) in the range of 25–900 °C at a heating rate of 15 K/min under the nitrogen atmosphere. X-ray photoelectron spectroscopy (XPS) was carried out with a Thermal Scientific K-Alpha instrument using to investigate the distribution of Ti, Ce, and Au in the  $\text{TiO}_2@\text{Au}@\text{CeO}_2$  hollow sphere. The UV–vis absorption spectra were measured using a spectrophotometer (UV–vis 2550, Shimadzu, Japan). The BET surface area measurement was obtained from  $\text{N}_2$  adsorption at 77 K over a relative pressure ( $P/P_0$ ) range from 0.01 to 0.99 on Micromeritics ASAP 2020 analyzer. The TOC reduction of trimesic acid was tested by Total organic carbon analyzer (TOC-VCPH, Shimadzu, Japan). The photoluminescence (PL) emission spectra of the samples were recorded to investigate the recombination of photo-generated electrons/holes in the photocatalysts.

### 2.5. Photocatalytic activity measurements

The photocatalysts ( $\text{CeO}_2$ ,  $\text{TiO}_2$ , P25,  $\text{CeO}_2/\text{Au}$ ,  $\text{TiO}_2/\text{Au}$ ,  $\text{TiO}_2@\text{CeO}_2$ ,  $\text{TiO}_2@\text{CeO}_2/\text{Au}$ ,  $\text{TiO}_2@\text{Au}@\text{CeO}_2$ , 30 mg) ( $50\text{ mL}$ ,  $5 \times 10^{-3}\text{ g/L}$ ) were stirred in the dark for 1 h to attain its adsorption/desorption equilibrium for methyl orange. Photocatalytic activities were tested by the degradation of methyl orange under visible light irradiation. As light source, a 350 W Xenon Short Arc Lamp (wavelength > 400 nm) equipped with a cutoff filter of 400 nm (UVIRCU400, CEAULIGHT) was located 10 cm above the liquid surface and the irradiation was  $2.86 \pm 0.05\text{ mW cm}^{-2}$  on the liquid surface, which was measured with a light dynamometer (TES-1333 solar power meter, China). The temperature of the reaction system was maintained as  $25^\circ\text{C} \pm 5^\circ\text{C}$  with cooling air and water. The concentration of methyl orange was determined by monitoring the absorbance of the methyl orange peak centered at 505 nm (UV–vis 2550, Shimadzu) as a function of irradiation time. The degradation rate was calculated using Eq. (1).

$$\text{Degradation rate} = \frac{(C_0 - C)}{C_0} \times 100\% \quad (1)$$

$C_0$  and  $C$  were the initial and residual pollutant concentration before and after visible light irradiation, respectively.

The first-order kinetic equation (Eq. (2)) was used to fit the experimental data:

$$\ln\left(\frac{C_0}{C}\right) = k_{\text{app}} \times t \quad (2)$$

$k_{\text{app}}$  was the reaction rate constant and  $t$  was the reaction time.

The photocatalysts ( $\text{TiO}_2@\text{CeO}_2$ ,  $\text{TiO}_2@\text{CeO}_2/\text{Au}$ ,  $\text{TiO}_2@\text{Au}@\text{CeO}_2$ , 30 mg) with trimesic acid ( $50\text{ mL}$ ,  $10 \times 10^{-3}\text{ g/L}$ ) were reacted with the same condition as methyl orange. After photo-degradation, the samples were collected and filtered, followed by the TOC reduction of trimesic acid was tested by Total organic carbon analyzer.

### 2.6. Photo-reduction of Cr(VI) measurements

Cr(VI) (100 mg/L, as stock solution) was prepared by dissolving  $\text{K}_2\text{Cr}_2\text{O}_7$  in ultrapure water and diluted to 5 mg/L for the photo-reduction experiment. The photocatalysts ( $\text{TiO}_2@\text{CeO}_2$ ,  $\text{TiO}_2@\text{CeO}_2/\text{Au}$ ,  $\text{TiO}_2@\text{Au}@\text{CeO}_2$ , 30 mg) with Cr(VI) ( $4.8\text{ }\mu\text{mol}$ ,  $\text{pH}=4.03$ ) in a quartz reactor (100 mL) were stirred in the dark for 1 h, its adsorption-desorption equilibrium was achieved, and then their photo-reduction performances were tested under the same conditions as photo-degradation. A UV–vis spectrophotometer (UV–vis 2550, Shimadzu, Japan) was used to determine the Cr(VI) concentration using the 1,5-diphenylcarbazide method [40].

## 3. Results and discussion

The double-shelled  $\text{TiO}_2@\text{CeO}_2$ ,  $\text{TiO}_2@\text{CeO}_2/\text{Au}$  and  $\text{TiO}_2@\text{Au}@\text{CeO}_2$  hollow spheres were prepared by a general “template + sol-gel + calcination” method (Scheme 2). Using methyl acrylate and sodium persulfate as surface active agents, smooth, anionic monodispersed PS spheres with diameters of 350 nm were prepared (see Fig. S1). The  $\text{TiO}_2$  shell,  $\text{CeO}_2$  shell and Au NPs were coated onto PS. According to the results of TG (see Fig. S2), the PS core could be removed by the calcination at 600 °C. The effect of calcination time on the structure and morphology of the  $\text{TiO}_2@\text{CeO}_2$  nanocomposites has been investigated. The structure of  $\text{TiO}_2@\text{CeO}_2$  hollow sphere was not changed and the hollow sphere size of  $\text{TiO}_2@\text{CeO}_2$  was uniformed by calcination at different times. However, if the firing time was too short, the crystallization of the  $\text{TiO}_2@\text{CeO}_2$  nanocomposites would be incomplete. If the firing time was too long, the coated  $\text{CeO}_2$  nanoparticles

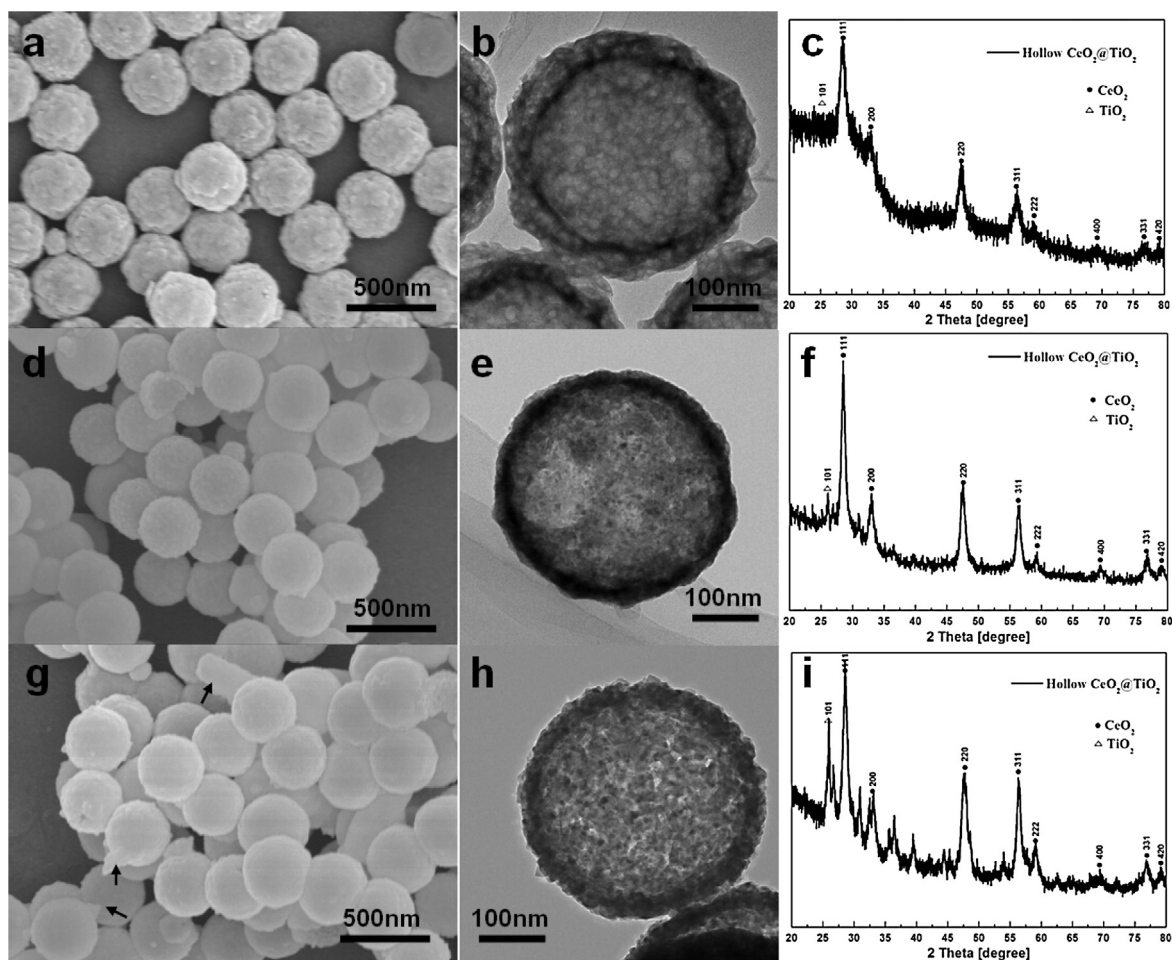


**Fig. 1.** The SEM, TEM and XRD images of double-shelled  $\text{TiO}_2@\text{CeO}_2$  hollow spheres synthesized by calcination of  $\text{PS}@\text{TiO}_2@\text{CeO}_2$  at  $600^\circ\text{C}$  about 3 h (a–c), 6 h (d–f) and 9 h (g–i).

in  $\text{TiO}_2@\text{CeO}_2$  nanocomposites would be partially detached. The conclusion was confirmed by the SEM, TEM and XRD images of  $\text{TiO}_2@\text{CeO}_2$  nanocomposites (see Fig. 1). So we choose calcined 6 h as a suitable calcined time to ensure that the next step of the study.

Because of abundant surface hydroxyl groups,  $\text{Ce}^{6+}$  cations from  $\text{CeN}_3\text{O}_9$  could be absorbed and then  $\text{CeO}_2$  was formed directly onto the surface of  $\text{PS}@\text{TiO}_2$  microspheres, resulting in the double-shelled structure. After calcination, the ultimate diameter of  $\text{TiO}_2@\text{CeO}_2$  nanocomposite was about 360 nm, which could be confirmed by the SEM and TEM (see Fig. 2a–d). TEM images confirmed a hollow in the  $\text{TiO}_2@\text{CeO}_2$  microspheres (Fig. 2c–d). A close inspection of the TEM image of  $\text{TiO}_2@\text{CeO}_2$  revealed the presence of individual nanoparticles on a thick and layered shell, and nanostructured hollow spheres. The formation of the junction between  $\text{TiO}_2$  and  $\text{CeO}_2$  could be confirmed by the HRTEM image (Fig. 2e). The types of lattice spacings (i.e., 0.351, 0.31, and 0.19 nm) were showed in Fig. 2e. Corresponding to the (101) planes of anatase  $\text{TiO}_2$ , the (111), and (220) crystallographic planes of  $\text{CeO}_2$ . The polycrystalline nature was also confirmed by the SAED measurements (Fig. 2f). According to the green, red and orange colored areas in HAADF-STEM mapping image (Fig. 2g). The  $\text{TiO}_2@\text{CeO}_2$  hollow sphere was comprised of “O”, “Ti” and “Ce” enriched area, i.e.,  $\text{TiO}_2$  shell and  $\text{CeO}_2$  shell. The hollow sphere of  $\text{TiO}_2@\text{CeO}_2$  was investigated by XRD analysis and the results were shown in Fig. 2h. The peak was indexed to the (101) planes of  $\text{TiO}_2$ , which were in good agreement with the standard pattern of anatase (JCPDS NO. 21-1272) [41]. The  $2\theta$  peaks were corresponded to the diffraction from the (111), (200), (220), (311), (222), (400), (331), and (420)

crystallographic planes of cubic phase of  $\text{CeO}_2$  (JCPDS NO. 34-0394) [42]. In the line scanning images of  $\text{TiO}_2@\text{CeO}_2$  (inset Fig. 3a), the distribution of Ti and Ce was hierarchical structure, suggesting that  $\text{TiO}_2@\text{CeO}_2$  was double-shelled hollow sphere. The nanocomposite of double-shelled  $\text{TiO}_2@\text{CeO}_2$  hollow spheres were composed of  $\text{TiO}_2$  shell and  $\text{CeO}_2$  shell, and the atomic ratio of  $\text{TiO}_2$ , and  $\text{CeO}_2$  were 17.47 and 21.93, respectively (Fig. 3b).

The XPS spectrum of  $\text{TiO}_2@\text{CeO}_2$  hollow sphere was shown in Fig. 4. The XPS peaks of  $\text{Ti } 2p_{3/2}$  and  $2p_{1/2}$  were located at about 458.5 eV and 464.2 eV with a good symmetry (Fig. 4a), indicating that there was  $\text{Ti}^{4+}$  in octahedral coordination with oxygen [43]. Moreover, the chemical environments for Ti and O<sub>L</sub> (Fig. 4b) were not changed, strongly suggesting that tungsten did not enter into the  $\text{TiO}_2$  crystal lattice under mild solvothermal conditions. Fig. 4c showed the peaks of  $\text{Ce } 3d_{3/2}$  and  $\text{Ce } 3d_{5/2}$  from XPS, which corresponded to the  $\text{CeO}_2$  layers in the  $\text{TiO}_2@\text{CeO}_2$  hollow sphere [8].

The diffuse reflectance UV–vis spectra of the prepared photocatalysts were shown in Fig. 5. The absorption edges of pure  $\text{TiO}_2$  hollow sphere was 385 nm, corresponding to the band gap of 3.2 eV. The result was similar to the reported in the literatures [44]. The absorption edge of  $\text{TiO}_2@\text{CeO}_2$  hollow sphere was 460 nm, the light absorption of  $\text{TiO}_2@\text{CeO}_2$  hollow sphere was stronger than that of  $\text{TiO}_2$  hollow sphere, i.e., the visible light-harvesting efficiency of  $\text{TiO}_2$  hollow sphere was improved by the combination of  $\text{CeO}_2$  shell.

To investigate the effect of the photocatalysts structure on photocatalytic activity, eight kinds of photocatalysts, including  $\text{CeO}_2$ ,  $\text{TiO}_2$ , P25,  $\text{CeO}_2/\text{Au}$ ,  $\text{TiO}_2/\text{Au}$ ,  $\text{TiO}_2@\text{CeO}_2$ ,  $\text{TiO}_2@\text{CeO}_2/\text{Au}$  and  $\text{TiO}_2@\text{Au}@\text{CeO}_2$  hollow sphere, were used for methyl orange photo-



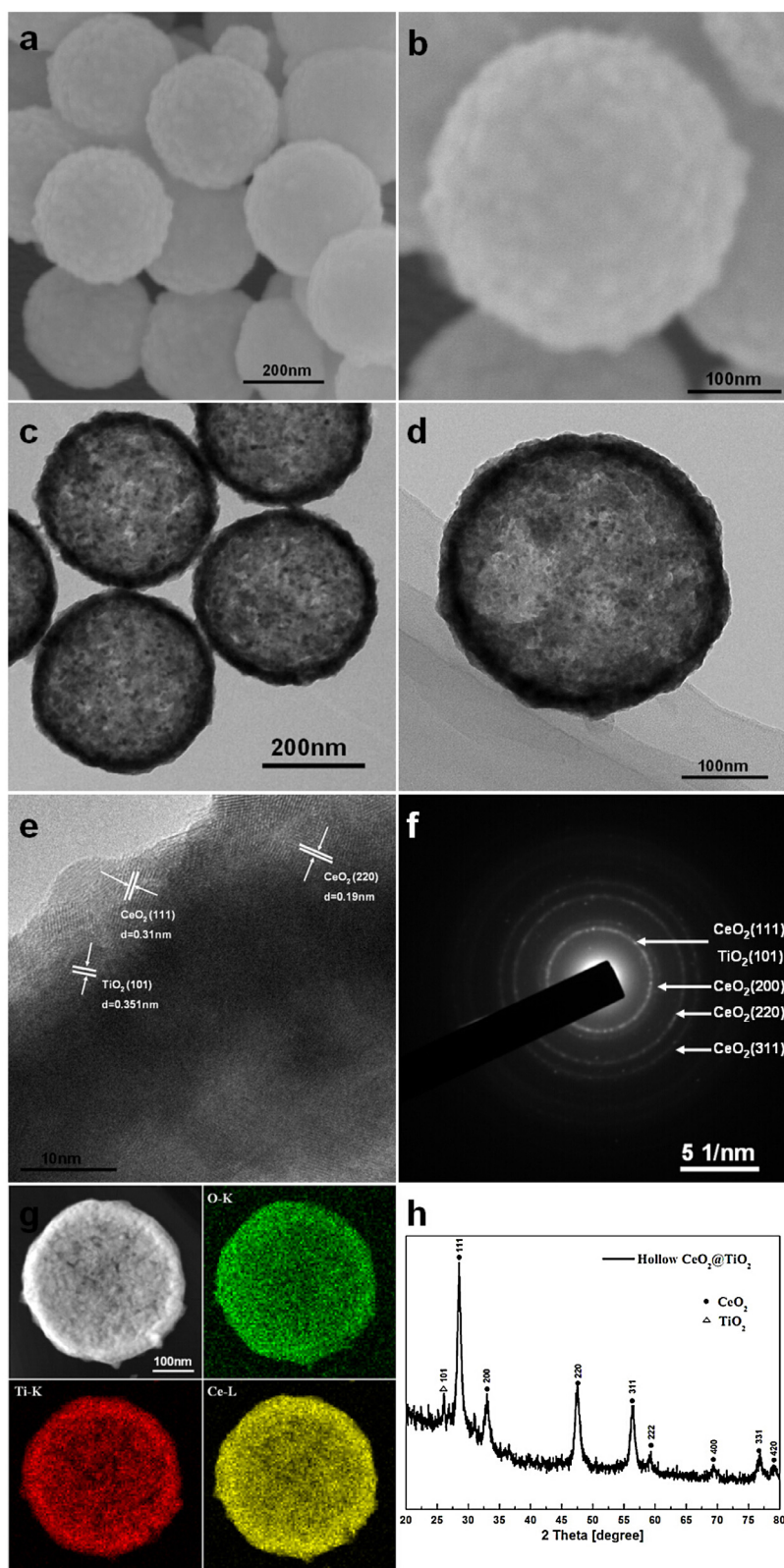


**Fig. 2.** (a and b) SEM images of double-shelled  $\text{TiO}_2@\text{CeO}_2$  hollow sphere, (c and d) TEM images of double-shelled  $\text{TiO}_2@\text{CeO}_2$  hollow sphere, (e) HRTEM images of double-shelled  $\text{TiO}_2@\text{CeO}_2$  hollow sphere, (f) SAED images of double-shelled  $\text{TiO}_2@\text{CeO}_2$  hollow sphere, (g) HAADF-STEM mapping image of double-shelled  $\text{TiO}_2@\text{CeO}_2$  hollow sphere, (h) XRD pattern of double-shelled  $\text{TiO}_2@\text{CeO}_2$  hollow sphere.

degradation under simulated sunlight irradiation for 120 min. The results were shown in Fig. 6 and Table 1. Although the  $\text{TiO}_2@\text{CeO}_2$  hollow sphere exhibited high photocatalytic activity, it was not enough. In order to further improve photo-degradation activ-

ity, Au NPs were deposited on the inner and outer layer surface of  $\text{TiO}_2@\text{CeO}_2$  hollow sphere by “template + sol-gel + calcination” method (Scheme 2). The photocatalytic activity of  $\text{TiO}_2@\text{Au}@\text{CeO}_2$  hollow sphere was higher than that of P25 and  $\text{TiO}_2$ . The photo-

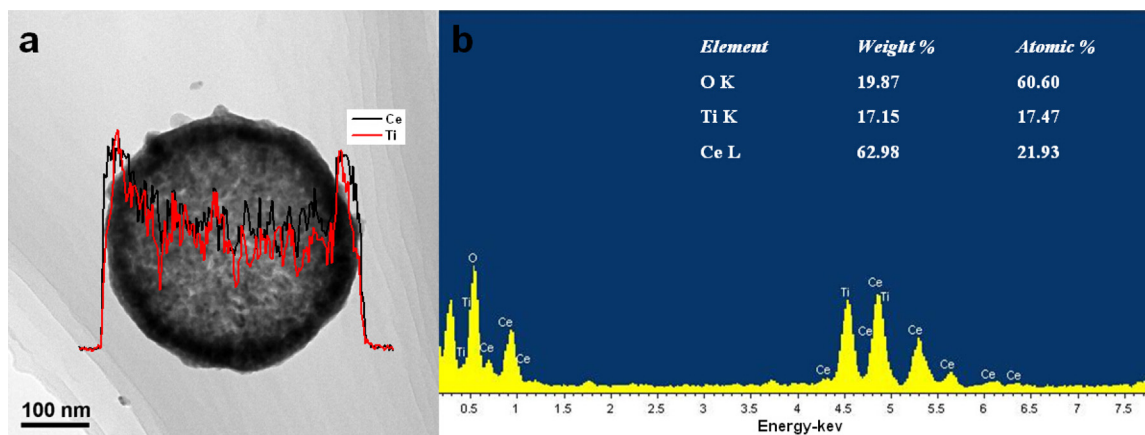


Fig. 3. (a) TEM images and (b) EDX of double-shelled  $\text{TiO}_2@\text{CeO}_2$  hollow sphere (the line scanning image of double-shelled  $\text{TiO}_2@\text{CeO}_2$  hollow spheres inset).

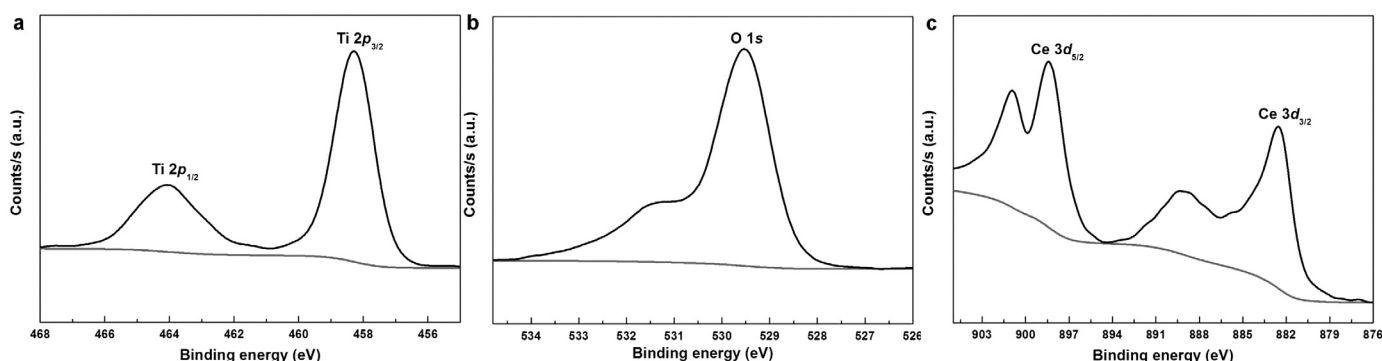


Fig. 4. The XPS peaks of (a) O 1s, (b) Ti 2p, and (c) Ce 3d of  $\text{TiO}_2@\text{CeO}_2$  hollow sphere.

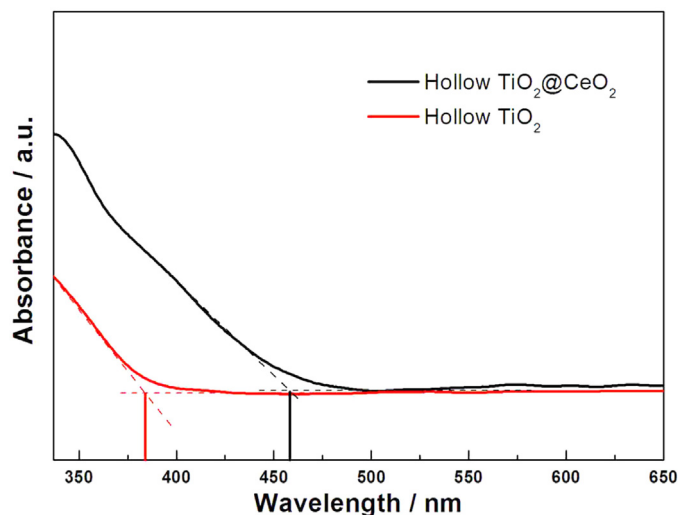


Fig. 5. Diffuse reflectance UV-vis spectra of hollow  $\text{TiO}_2$  and hollow  $\text{TiO}_2@\text{CeO}_2$  microspheres.

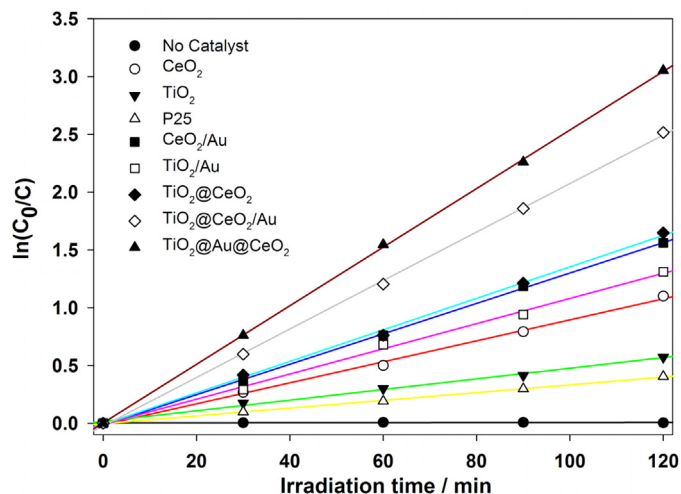


Fig. 6. Linear transform  $\ln(C_0/C) = f(t)$  of the kinetic curves of methyl orange by  $\text{CeO}_2$ , hollow  $\text{TiO}_2$ , P25,  $\text{CeO}_2/\text{Au}$ , hollow  $\text{TiO}_2/\text{Au}$ , double-shelled  $\text{TiO}_2@\text{CeO}_2$ , double-shelled  $\text{TiO}_2@\text{CeO}_2/\text{Au}$ , or double-shelled  $\text{TiO}_2@\text{Au}@\text{CeO}_2$  hollow sphere under visible light irradiation.

degradation rate of 95% for methyl orange was achieved by  $\text{TiO}_2@\text{Au}@\text{CeO}_2$ , which exhibited an increase of 64% and 54% compared to Degussa P25 and  $\text{TiO}_2$ , respectively. Meanwhile, the linear relationship between  $\ln(C_0/C)$  and  $t$  indicated that the photo-degradation reactions followed pseudo-first-order kinetics (see Fig. 6 and Table 1) with rate constants (0.0091, 0.0046, 0.0034, 0.013, 0.011, 0.014, 0.021 and 0.026  $\text{min}^{-1}$ ) for  $\text{CeO}_2$ , hollow  $\text{TiO}_2$ , P25,  $\text{CeO}_2/\text{Au}$ ,  $\text{TiO}_2/\text{Au}$ , or double-shelled  $\text{TiO}_2@\text{CeO}_2$ , double-

shelled  $\text{TiO}_2@\text{CeO}_2/\text{Au}$  and double-shelled  $\text{TiO}_2@\text{Au}@\text{CeO}_2$  hollow sphere, respectively.

TEM images confirmed Au NPs in the  $\text{TiO}_2@\text{CeO}_2$  microspheres (Figs. 7 and 8, Figs. S3 and S4). The formation of the junction between  $\text{TiO}_2$ ,  $\text{CeO}_2$  and Au NPs could be confirmed by the HRTEM images and HAADF-STEM images (Figs. 7 and 8). The Au NPs was coated outer face in the double-shelled  $\text{TiO}_2@\text{CeO}_2/\text{Au}$  hollow sphere and the Au NPs was sandwiched between the double shell

**Table 1**

Visible light photo-degradation rate constant  $k$  ( $\text{min}^{-1}$ ) and correlation coefficient  $R^2$  for  $\text{CeO}_2$ , hollow  $\text{TiO}_2$ , P25,  $\text{CeO}_2/\text{Au}$ , hollow  $\text{TiO}_2/\text{Au}$ , double-shelled  $\text{TiO}_2@\text{CeO}_2$ , double-shelled  $\text{TiO}_2@\text{CeO}_2/\text{Au}$ , or double-shelled  $\text{TiO}_2@\text{Au}@\text{CeO}_2$  hollow sphere.

Sample	$k$ ( $\text{min}^{-1}$ )	$R^2$
	methyl orange	methyl orange
$\text{CeO}_2$	0.0091	0.997
$\text{TiO}_2$	0.0046	0.995
P25	0.0034	0.999
$\text{CeO}_2/\text{Au}$	0.013	0.999
$\text{TiO}_2/\text{Au}$	0.011	0.996
double-shelled $\text{CeO}_2@\text{TiO}_2$	0.014	0.998
double-shelled $\text{CeO}_2@\text{TiO}_2/\text{Au}$	0.021	0.998
double-shelled $\text{CeO}_2@\text{Au}@\text{TiO}_2$	0.026	0.999

of  $\text{TiO}_2$  and  $\text{CeO}_2$ , respectively. The XPS spectra of  $\text{TiO}_2@\text{Au}@\text{CeO}_2$  (Fig. S4) showed the peaks of  $\text{Au } 4f_{7/2}$  and  $\text{Au } 4f_{5/2}$  centered at 84.2 and 87.8 eV, respectively. The spin energy separation of 3.6 eV was in good agreement with the reported data of  $\text{Au } 4f_{7/2}$  and  $\text{Au } 4f_{5/2}$  in Au NPs [37].

The visible-light for methyl orange photo-degradation rate of  $\text{TiO}_2@\text{Au}@\text{CeO}_2$  was 95%, which exhibited an increase of 16% compared with  $\text{TiO}_2@\text{CeO}_2$ , because Au NPs in the sandwich layer could effectively reduce the recombination of photo-induced electrons and holes. The photocatalytic activity was in the order of  $\text{TiO}_2@\text{Au}@\text{CeO}_2 > \text{TiO}_2@\text{CeO}_2/\text{Au} > \text{TiO}_2@\text{CeO}_2$ . Comparison of the photocatalytic activity of different  $\text{TiO}_2$ -based photocatalysts (Table S1), the synergistic effect of  $\text{CeO}_2$  shell and Au nanoparticles as co-catalysts for enhancing visible-light-driven photocatalytic activity of  $\text{TiO}_2$  hollow spheres was confirmed. The electron-hole separation could be facilitated through the unique hierarchically mesoporous hollow structure and sandwich structure. As shown in the diffuse reflectance UV–vis spectra (see Fig. S5), among the  $\text{TiO}_2@\text{CeO}_2$ ,  $\text{TiO}_2@\text{CeO}_2/\text{Au}$  and  $\text{TiO}_2@\text{Au}@\text{CeO}_2$  hollow sphere, the band at 550–700 nm was likely coming from Au NPs. When Au NPs was encapsulated in  $\text{TiO}_2@\text{CeO}_2/\text{Au}$  and  $\text{TiO}_2@\text{Au}@\text{CeO}_2$  hollow sphere, its visible light-harvesting was obtained in  $\text{TiO}_2@\text{CeO}_2/\text{Au}$  and  $\text{TiO}_2@\text{Au}@\text{CeO}_2$  hollow sphere. The stability of  $\text{TiO}_2@\text{Au}@\text{CeO}_2$

as photocatalyst was enough, because no obvious decrease in photocatalytic activity on degradation of methyl orange was observed after three cycles (see Fig. S6, Fig. 9a, b). However, the visible-light for methyl orange photo-degradation rate of  $\text{TiO}_2@\text{CeO}_2/\text{Au}$  was reduced from 91% to 71% after three cycles, which may be ascribed the stability of  $\text{TiO}_2@\text{CeO}_2/\text{Au}$ . The Au NPs was part started from  $\text{TiO}_2@\text{CeO}_2/\text{Au}$  on degradation of methyl orange after three cycles (see Fig. S6, Fig. 9c, d).

The photo-luminescence (PL) emission mainly resulted from the recombination of excited electrons and holes. Among the five photocatalysts, the PL intensity of  $\text{TiO}_2@\text{Au}@\text{CeO}_2$  was the lowest (see Fig. S7), which indicated its separation efficiency was the highest. To further investigate the influence of controllable location of the noble metals as co-catalysts for enhancing photocatalytic activity. The  $\text{TiO}_2@\text{CeO}_2$ ,  $\text{TiO}_2@\text{CeO}_2/\text{Au}$ , and  $\text{TiO}_2@\text{Au}@\text{CeO}_2$  hollow spheres were used for trimesic acid photo-degradation under simulated sunlight irradiation for 180 min. The results were shown in Fig. 10. A similar conclusion could be obtained by considering the total organic carbon content before and after the photo-degradation (Table S2). The TOC reduction of trimesic acid for  $\text{TiO}_2@\text{CeO}_2$ ,  $\text{TiO}_2@\text{CeO}_2/\text{Au}$  and  $\text{TiO}_2@\text{Au}@\text{CeO}_2$  were 46%, 52% and 58%, respectively. The photocatalytic rate of the  $\text{TiO}_2@\text{Au}@\text{CeO}_2$  hollow sphere increased obviously as compared to the others, suggesting that the  $\text{TiO}_2@\text{Au}@\text{CeO}_2$  hollow sphere provided appropriate electronic channel and accelerated the photo-generated electron-hole separation. The specific surface area and average pore size of double-shelled  $\text{TiO}_2@\text{Au}@\text{CeO}_2$  hollow sphere were  $32 \text{ m}^2 \text{ g}^{-1}$  and 20.0 nm (see Fig. S8 and Table S3), indicating  $\text{TiO}_2@\text{Au}@\text{CeO}_2$  hollow sphere was also a typical mesoporous material. The apparent quantum efficiency (AQE) of  $\text{TiO}_2@\text{CeO}_2$ ,  $\text{TiO}_2@\text{CeO}_2/\text{Au}$  and  $\text{TiO}_2@\text{Au}@\text{CeO}_2$  was evaluated by the photo-reduction of  $\text{Cr(VI)}$  (initially  $4.8 \mu\text{mol}$ ) in aqueous suspensions (see Fig. 11), i.e.,  $\text{Cr(VI)}$  was used as an electron acceptor. After visible light irradiation for 5 h, the photo-reduction rate of  $\text{Cr(VI)}$  for  $\text{TiO}_2@\text{Au}@\text{CeO}_2$  was 79%, which exhibited an increase of 19% and 7% compared with  $\text{TiO}_2@\text{CeO}_2$  and  $\text{TiO}_2@\text{CeO}_2/\text{Au}$  (see Fig. S9). The  $\text{Cr(VI)}$  photo-reduction rates were 0.576, 0.691 and  $0.758 \mu\text{mol h}^{-1}$

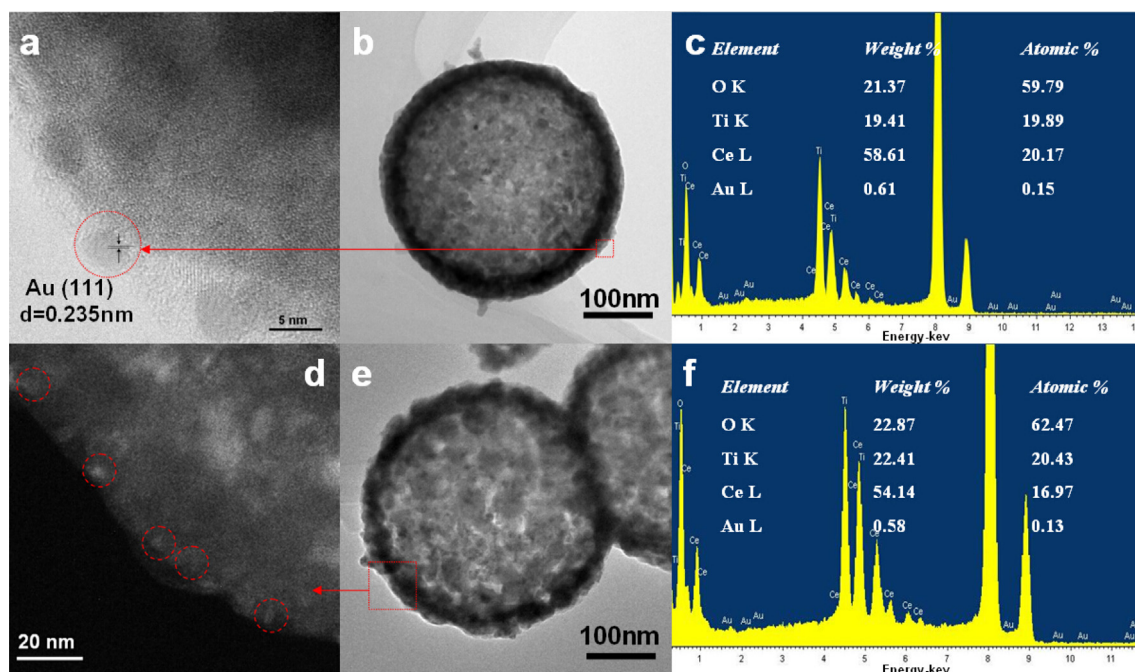


**Fig. 7.** (a) HRTEM images, (b) TEM images and (c) EDX of double-shelled  $\text{TiO}_2@\text{CeO}_2/\text{Au}$  hollow sphere, (d) HAADF-STEM images, (e) TEM images and (f) EDX of double-shelled  $\text{TiO}_2@\text{Au}@\text{CeO}_2$  hollow sphere.



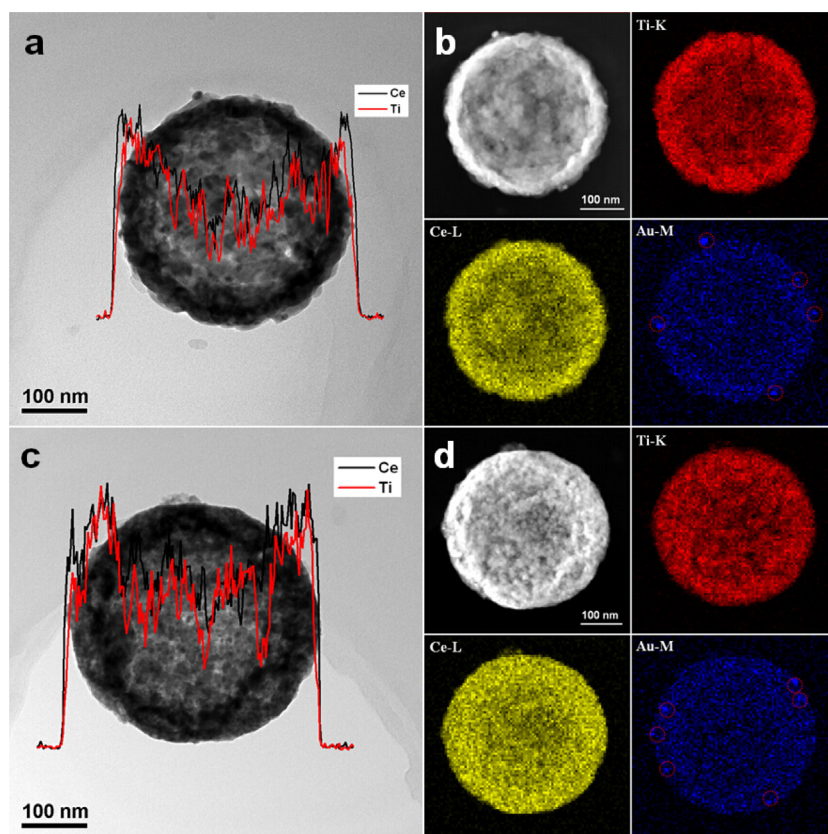


**Fig. 8.** (a) TEM images and the line scanning image and (b) HAADF-STEM mapping image of double-shelled  $\text{TiO}_2@\text{CeO}_2/\text{Au}$  hollow sphere, (c) TEM images and the line scanning image and (d) HAADF-STEM mapping image of double-shelled  $\text{TiO}_2@\text{Au}@\text{CeO}_2$  hollow sphere.

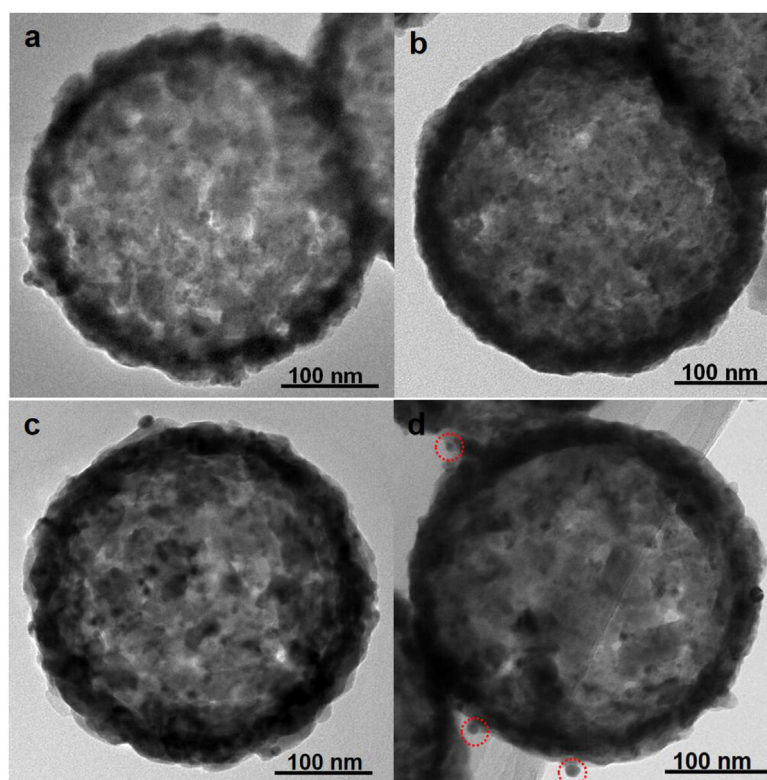


**Fig. 9.** TEM images of  $\text{TiO}_2@\text{Au}@\text{CeO}_2$  hollow sphere before (a) and after (b) photo-degradation, TEM images of  $\text{TiO}_2@\text{CeO}_2/\text{Au}$  hollow sphere before (c) and after (d) photo-degradation.



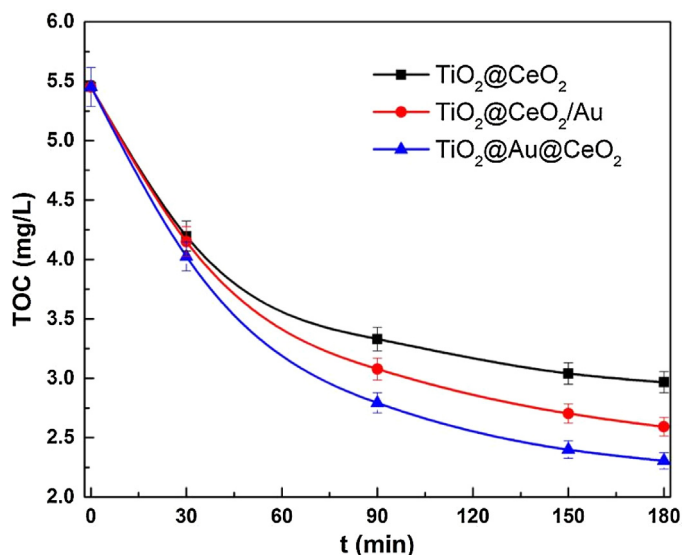


Fig. 10. The total organic carbon content of trimesic acid before and after the photo-degradation for TiO<sub>2</sub>@CeO<sub>2</sub>, TiO<sub>2</sub>@CeO<sub>2</sub>/Au and TiO<sub>2</sub>@Au@CeO<sub>2</sub>.

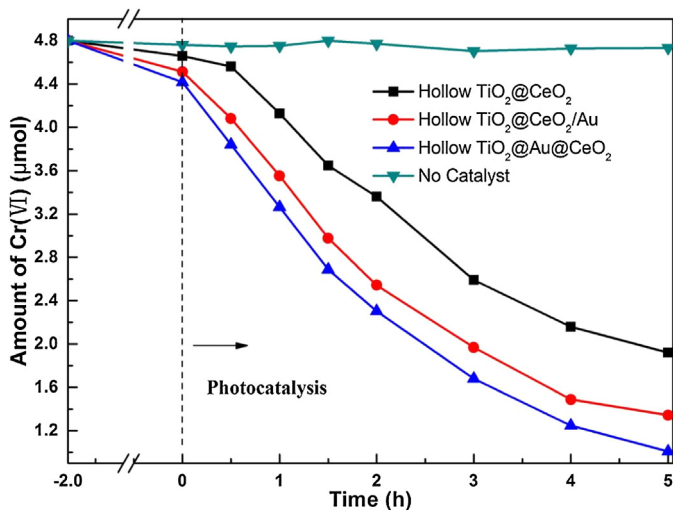
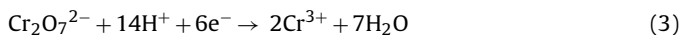


Fig. 11. Time courses of the amounts of Cr(VI) in aqueous suspensions by TiO<sub>2</sub>@CeO<sub>2</sub>, TiO<sub>2</sub>@CeO<sub>2</sub>/Au and TiO<sub>2</sub>@Au@CeO<sub>2</sub> under visible light irradiation.

for TiO<sub>2</sub>@CeO<sub>2</sub>, TiO<sub>2</sub>@CeO<sub>2</sub>/Au and TiO<sub>2</sub>@Au@CeO<sub>2</sub>, respectively (see in Fig. 12).



$$\text{AQE} = \frac{3 \times \text{the amount of Cr(VI) reduced}}{\text{the amount of incident photons}} \times 100 \quad (4)$$

#### 4. Conclusions

A new nanocomposite with double-shelled, nanostructured hollow spheres, and supported Au nanoparticles (NPs) was designed as a high-performance visible-light-driven photocatalyst, using a sacrificial templates route. The synergistic effect of coupling TiO<sub>2</sub> hollow spheres with CeO<sub>2</sub> shell (as photocatalyst and oxygen buffer) and Au NPs (as co-catalyst) on photocatalytic performance was proved by this paper. The heterogeneous photocatalytic activity could be improved by hollow sphere structure, controllable location of co-catalyst (e.g., Au nanoparticles), and shell-shell combination of photocatalyst with different band gap. The morphology of the hollow TiO<sub>2</sub>@Au@CeO<sub>2</sub> was uniform and its synthesis pro-

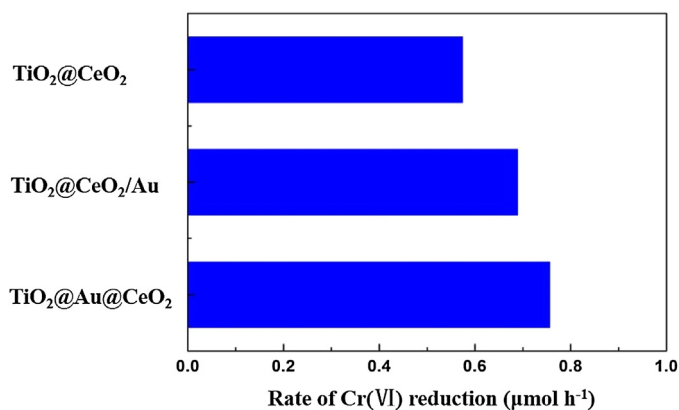


Fig. 12. Rates of Cr(VI) photo-reduction in aqueous suspensions by TiO<sub>2</sub>@CeO<sub>2</sub>, TiO<sub>2</sub>@CeO<sub>2</sub>/Au and TiO<sub>2</sub>@Au@CeO<sub>2</sub> under visible light irradiation.

cedure was simple. This photocatalyst structure was unique and novel, which efficient catalytic performance was demonstrated by the photocatalytic decomposition of organic pollutants.

#### Acknowledgements

This work is supported by the National Natural Science Foundation of China (21175115 and 21475055, S.X.L.), the Program for New Century Excellent Talents in University (NCET-11 0904, S.X.L.).

#### Appendix A. Supplementary data

Supplementary data associated with this article can be found, in the online version, at <http://dx.doi.org/10.1016/j.apcatb.2016.08.003>.

#### References

- [1] J. Di, J. Xia, Y. Ge, H. Li, H. Ji, H. Xu, Q. Zhang, H. Li, M. Li, Appl. Catal. B 168 (2015) 51–61.
- [2] X. Yang, J. Qin, Y. Jiang, K. Chen, X. Yan, D. Zhang, R. Li, H. Tang, Appl. Catal. B 166 (2015) 231–240.
- [3] K. Li, Z. Zeng, L. Yan, M. Huo, Y. Guo, S. Luo, X. Luo, Appl. Catal. B 187 (2016) 269–280.
- [4] J.-J. Chen, W.-K. Wang, W.-W. Li, D.-N. Pei, H.-Q. Yu, ACS Appl. Mater. Interfaces 7 (2015) 12671–12678.
- [5] C.-C. Wang, J.-R. Li, X.-L. Lv, Y.-Q. Zhang, G. Guo, Energy Environ. Sci. 7 (2014) 2831–2867.
- [6] B. Qiu, M. Xing, J. Zhang, J. Am. Chem. Soc. 136 (2014) 5852–5855.
- [7] X. Luo, F. Deng, L. Min, S. Luo, B. Guo, G. Zeng, C. Au, Environ. Sci. Technol. 47 (2013) 7404–7412.
- [8] M.J. Munˆoz-Batista, M.N. Gómez-Cerezo, A. Kubacka, D. Tudela, M. Fernández-García, ACS Catal. 4 (2013) 63–72.
- [9] H. Sun, S. Liu, S. Liu, S. Wang, Appl. Catal. B 146 (2014) 162–168.
- [10] Y. Hu, X. Gao, L. Yu, Y. Wang, J. Ning, S. Xu, X.W.D. Lou, Angew. Chem. Int. Ed. 125 (2013) 5746–5749.
- [11] S. Obregón, A. Caballero, G. Colón, Appl. Catal. B 117 (2012) 59–66.
- [12] C. Yu, K. Yang, Y. Xie, Q. Fan, C.Y. Jimmy, Q. Shu, C. Wang, Nanoscale 5 (2013) 2142–2151.
- [13] D. Li, Q. Qin, X. Duan, J. Yang, W. Guo, W. Zheng, ACS Appl. Mater. Interfaces 5 (2013) 9095–9100.
- [14] J. Hu, M. Chen, X. Fang, L. Wu, Chem. Soc. Rev. 40 (2011) 5472–5491.
- [15] J. Cai, X. Wu, S. Li, F. Zheng, L. Zhu, Z. Lai, ACS Appl. Mater. Interfaces 7 (2015) 3764–3772.
- [16] X. Liu, K. Zhou, L. Wang, B. Wang, Y. Li, J. Am. Chem. Soc. 131 (2009) 3140–3141.
- [17] F. Esch, S. Fabris, L. Zhou, T. Montini, C. Africh, P. Fornasiero, G. Comelli, R. Rosei, Science 309 (2005) 752–755.
- [18] X.H. Guo, C.C. Mao, J. Zhang, J. Huang, W.N. Wang, Y.H. Deng, Y.Y. Wang, Y. Cao, W.X. Huang, S.H. Yu, Small 8 (2012) 1515–1520.
- [19] J. Qi, J. Chen, G. Li, S. Li, Y. Gao, Z. Tang, Energy Environ. Sci. 5 (2012) 8937–8941.
- [20] Q. Xiang, J. Yu, M. Jaroniec, J. Am. Chem. Soc. 134 (2012) 6575–6578.
- [21] H.B. Wu, H.H. Hng, X.W.D. Lou, Adv. Mater. 24 (2012) 2567–2571.
- [22] F. Zuo, K. Bozhilov, R.J. Dillon, L. Wang, P. Smith, X. Zhao, C. Bardeen, P. Feng, Angew. Chem. Int. Ed. 124 (2012) 6327–6330.

- [23] D.N. Correa, J.M. de Souza e Silva, E.B. Santos, F.A. Sigoli, A.G. Souza Filho, I.O. Mazali, *J. Phys. Chem. C* 115 (2011) 10380–10387.
- [24] H. Eskandarloo, A. Badiei, M.A. Behnajady, *Ind. Eng. Chem. Res.* 53 (2014) 7847–7855.
- [25] I. Alessandri, M. Zucca, M. Ferroni, E. Bontempi, L.E. Depero, *Small* 5 (2009) 336–340.
- [26] J. Jiao, Y. Wei, Z. Zhao, J. Liu, J. Li, A. Duan, G. Jiang, *Ind. Eng. Chem. Res.* 53 (2014) 17345–17354.
- [27] T. Cao, Y. Li, C. Wang, L. Wei, C. Shao, Y. Liu, *J. Sol-Gel Sci. Technol.* 55 (2010) 105–110.
- [28] B. Jiang, S. Zhang, X. Guo, B. Jin, Y. Tian, *Appl. Surf. Sci.* 255 (2009) 5975–5978.
- [29] B. Liu, X. Zhao, N. Zhang, Q. Zhao, X. He, J. Feng, *Surf. Sci.* 595 (2005) 203–211.
- [30] P. Li, Y. Xin, Q. Li, Z. Wang, Z. Zhang, L. Zheng, *Environ. Sci. Technol.* 46 (2012) 9600–9605.
- [31] B. Murugan, A. Ramaswamy, *J. Phys. Chem. C* 112 (2008) 20429–20442.
- [32] R. Si, J. Tao, J. Evans, J.B. Park, L. Barrio, J.C. Hanson, Y. Zhu, J. Hrbek, J.A. Rodriguez, *J. Phys. Chem. C* 116 (2012) 23547–23555.
- [33] J. Fang, H. Bao, B. He, F. Wang, D. Si, Z. Jiang, Z. Pan, S. Wei, W. Huang, *J. Phys. Chem. C* 111 (2007) 19078–19085.
- [34] J. Du, J. Qi, D. Wang, Z. Tang, *Energy Environ. Sci.* 5 (2012) 6914–6918.
- [35] M.M. Khan, S.A. Ansari, M.O. Ansari, B. Min, J. Lee, M.H. Cho, *J. Phys. Chem. C* 118 (2014) 9477–9484.
- [36] J. Chen, D. Wang, J. Qi, G. Li, F. Zheng, S. Li, H. Zhao, Z. Tang, *Small* 11 (2015) 420–425.
- [37] J. Cai, X. Wu, S. Li, F. Zheng, *ACS Sustain. Chem. Eng.* 4 (2016) 1581–1590.
- [38] S. Li, J. Cai, X. Wu, F. Zheng, X. Lin, W. Liang, J. Chen, J. Zheng, Z. Lai, T. Chen, *Appl. Catal. B* 160 (2014) 279–285.
- [39] S. Li, J. Chen, F. Zheng, Y. Li, F. Huang, *Nanoscale* 5 (2013) 12150–12155.
- [40] L. Clesceri, A. Greenberg, A. Eaton, *Standard Methods for the Examination of Water and Wastewater*, 20th ed., APHA, Washington, DC, 1998.
- [41] J. Yu, J. Low, W. Xiao, P. Zhou, M. Jaroniec, *J. Am. Chem. Soc.* 136 (2014) 8839–8842.
- [42] Q. Xie, Y. Zhao, H. Guo, A. Lu, X. Zhang, L. Wang, M.-S. Chen, D.-L. Peng, *ACS Appl. Mater. Interfaces* 6 (2013) 421–428.
- [43] J. Zhuang, Q. Tian, H. Zhou, Q. Liu, P. Liu, H. Zhong, *J. Mater. Chem.* 22 (2012) 7036–7042.
- [44] S. Shang, X. Jiao, D. Chen, *ACS Appl. Mater. Interfaces* 4 (2012) 860–865.